

RESEARCH ARTICLE

10.1002/2014JB011009

Key Points:

- We performed field experiments in the El Tatio Geyser Field, Chile
- Observations reveal a geyser having two eruption styles with regular intervals
- Interaction between two water reservoirs can explain this behavior

Supporting Information:

- Readme
- Movie S1
- Movie S2

Correspondence to:

A. Namiki,
namiki@eps.s.u-tokyo.ac.jp

Citation:

Namiki, A., C. Muñoz-Saez, and M. Manga (2014), El Cobreloa: A geyser with two distinct eruption styles, *J. Geophys. Res. Solid Earth*, 119, doi:10.1002/2014JB011009.

Received 6 FEB 2014

Accepted 19 JUL 2014

Accepted article online 24 JUL 2014

El Cobreloa: A geyser with two distinct eruption styles

Atsuko Namiki¹, Carolina Muñoz-Saez², and Michael Manga²

¹Department of Earth and Planetary Science, University of Tokyo, Tokyo, Japan, ²Department of Earth and Planetary Science, University of California, Berkeley, California, USA

Abstract We performed field measurements at a geyser nicknamed “El Cobreloa,” located in the El Tatio Geyser Field, Northern Andes, Chile. The El Cobreloa geyser has two distinct eruption styles: minor eruptions and more energetic and long-lived major eruptions. Minor eruptions splash hot water intermittently over an approximately 4 min time period. Major eruptions begin with an eruption style similar to minor eruptions, but then transition to a voluminous liquid water-dominated eruption, and finally end with energetic steam discharge that continues for approximately 1 h. We calculated eruption intervals by visual observations, acoustic measurements, and ground temperature measurements and found that each eruption style has a regular interval: 4 h and 40 min for major eruptions and ~14 min for minor eruptions. Eruptions of El Cobreloa and geochemical measurements suggest interaction of three water sources. The geyser reservoir, connected to the surface by a conduit, is recharged by a deep, hot aquifer. More deeply derived magmatic fluids heat the reservoir. Boiling in the reservoir releases steam and hot liquid water to the overlying conduit, causing minor eruptions, and heating the water in the conduit. Eventually the water in the conduit becomes warm enough to boil, leading to a steam-dominated eruption that empties the conduit. The conduit is then recharged by a shallow, colder aquifer, and the eruption cycle begins anew. We develop a model for minor eruptions which heat the water in the conduit. El Cobreloa provides insight into how small eruptions prepare the geyser system for large eruptions.

1. Introduction

Geyser eruptions capture the imagination of the millions of visitors who watch them erupt [Bryan, 2005]. Their eruption mechanisms are also of scientific interest because they reveal some of the thermal and mechanical processes that occur in geothermal systems [Ingebritsen and Rojstaczer, 1993], are sometimes viewed as an analogue to volcanic eruptions [e.g., Kieffer, 1989], and document fundamental thermodynamic process inside planets [e.g., Lu and Kieffer, 2009]. A basic sequence of events characterizes an eruption: hot water fills a chamber or reservoir, vaporization increases the fluid volume, and then eruption occurs. The eruption interval is governed by the time required to fill the chamber and heat the water in the chamber [Ingebritsen and Rojstaczer, 1993; Kedar et al., 1998; O'Hara and Esawi, 2013]. The heating of cold water filling the chamber may occur by recharge of warmer liquid water and steam [Steinberg et al., 1981], and this recharge can be monitored by pressure measurements in the geyser conduit [Shteinberg et al., 2013]. Measurements of ground tilt during an eruption cycle document the recharge and discharge of the geyser system [Nishimura et al., 2006; Rudolph et al., 2012]. Similar processes and periodic eruptions occur in laboratory models of geysers [Steinberg et al., 1982; Toramaru and Maeda, 2013].

The frequency of geyser eruption is sometimes sensitive to external influences [Rojstaczer et al., 2003; Hurwitz et al., 2008], especially air temperature for geysers with a large pool at the surface [Hurwitz et al., 2014] and earthquakes [Husen et al., 2004; Manga and Brodsky, 2006]. The sensitivity to air temperature is consistent with the need to warm water in the geyser system to initiate an eruption. The sensitivity to earthquakes suggests that the geometry of the chamber and permeability surrounding the chamber have significant effects on eruption frequencies [Ingebritsen and Rojstaczer, 1993, 1996] because earthquakes can alter, at least temporarily, permeability [Manga et al., 2012]. Relative permeability depends on the volumetric liquid saturation and influences the periodicity [Ingebritsen and Rojstaczer, 1996]. The importance of two-phase flow in a porous media on hydrothermal systems has been confirmed experimentally [Vandemeulebrouck et al., 2005], and the two-phase flow excites acoustic emissions that are recorded at geysers [Kieffer, 1984; Kedar et al., 1996; Vandemeulebrouck et al., 2010; Cros et al., 2011].

The most direct insight into geyser conduits is provided by direct observation: at Old Faithful, Yellowstone National Park, the uppermost part of the conduit (<17 m) is an irregular, elongated fissure-like channel

[Hutchinson *et al.*, 1997]. Large underground cavities are also observed visually [Belousov *et al.*, 2013] and identified with hydrothermal tremor [Vandemeulebrouck *et al.*, 2013].

The eruption sequence of geysers is typified by Old Faithful and Lone Star geysers, Yellowstone National Park [Kieffer, 1989; Karlstrom *et al.*, 2013]: an eruption begins with “preplay” in which water is intermittently ejected prior to the actual eruption; an eruption column then develops and maintains a near constant height; the column height then decreases and eruption ends. The eruption is typically liquid-dominated to begin and steam-dominated near the end. There is, however, great variability in all aspects of geyser eruptions, including the interval between eruptions, the duration of eruption, the vigor or existence of preplay, and the height of the eruption.

In order to better characterize the variability of eruption style and understand the controls on eruption processes, we performed a set of field experiments at the El Tatio geyser field, Chile, where there are more than 100 episodically erupting springs. This geyser field has been explored to assess its potential for electric power generation, thus extensive geochemical and geological measurements exist [e.g., Cusicanqui *et al.*, 1975; Giggerbach, 1978; Cortecci *et al.*, 2005; Tassi *et al.*, 2010] to complement our surface observations. The geothermal fluid in El Tatio has high chloride concentration and can be interpreted as admixtures of meteoric, hydrothermal and magmatic water which experience loss of vapor [Cusicanqui *et al.*, 1975; Cortecci *et al.*, 2005]. The high $^3\text{He}/^4\text{He}$ ratio and negative $\delta^{13}\text{C}$ indicate a mantle gas contribution to the geothermal fluids [Urzua *et al.*, 2002; Cortecci *et al.*, 2005; Tassi *et al.*, 2005, 2010]. Here we focus on a geyser named El Cobreloa, which has two distinct eruption styles and eruption intervals.

2. Location and Geological Characteristics

The El Tatio Geyser Field is located in the Northern Andes, Chile (inset of Figure 1a). The geyser field is at high altitude, 4200–4300 m, so that the boiling temperature of water is approximately 86.6°C. The geothermal field is located in a region with Holocene volcanism, dominated by ignimbrites and lava domes (Figure 1a).

The deeper magmatic systems responsible for this volcanism are the heat sources for the geothermal systems. Most of the surface geothermal manifestations such as hot springs, fumaroles, and geysers are located in the hanging wall of the El Tatio half graben [Lahsen, 1976] and are concentrated in valley bottoms and where faults reach the surface.

Thirteen exploration and production wells were drilled between 1969 and 1974, reaching depths up to 1800 m and temperatures up to 250°C. The locations of some of wells are shown in Figure 1a. The El Cobreloa geyser is located close to well 2. The maximum temperature measured in well 2 was 226°C, and the maximum depth was 652 m. From geological studies, resistivity measurements and logging the geothermal wells, Healy and Hochstein [1973] generated the geological cross section shown in Figure 1b. Hot water flows within the permeable ignimbrites of the Puripicar Formation and its underlying layer [Healy and Hochstein, 1973; Lahsen, 1976]. The impermeable Tucle tuff caps this hot aquifer and separates it from a colder aquifer in the overlying dacite layer [Healy and Hochstein, 1973; Cusicanqui *et al.*, 1975; Cortecci *et al.*, 2005].

The chemistry of well discharges and of spring water is summarized in Cusicanqui *et al.* [1975]. At the initial opening of wells 2 and 9, the chloride concentrations of discharged water were considerably higher than those in any spring waters. Downhole sampling of waters at different depths in the wells shows that, in well 2, saturated brine with a density of 1200 kg m⁻³ exists at a depth below approximately 600 m. The well waters are compositionally similar to the spring waters and can be related chemically to a single parent water. Cusicanqui *et al.* [1975] compiled the water temperatures estimated by silica and Na:K geothermometry and the deep chloride concentrations obtained by surface sampling and downhole sampling, and showed the effect of boiling and dilution on the waters. They suggested that parent water entering the El Tatio system has a temperature of approximately 263°C. Downhole samples collected in well 7 showed that the water entering the well during discharge has boiled before reaching the well. The steam escapes into overlying formations and does not discharge from the well.

The geochemical features of the fluid discharge were recently reexamined to evaluate the potential of the geothermal system. Geothermometry based both on the Na:K ratio and gas in the H₂O-CO₂-H₂-CO-CH₄ system suggests that the temperature of source water in El Tatio is approximately 270°C [Cortecci *et al.*, 2005; Tassi *et al.*, 2010]. Isotope measurements show elevated $^3\text{He}/^4\text{He}$ ratios and low $\delta^{13}\text{C}$, implying input of magmatic gases and fluids to the discharged water [Urzua *et al.*, 2002; Cortecci *et al.*, 2005; Tassi *et al.*, 2005, 2010].

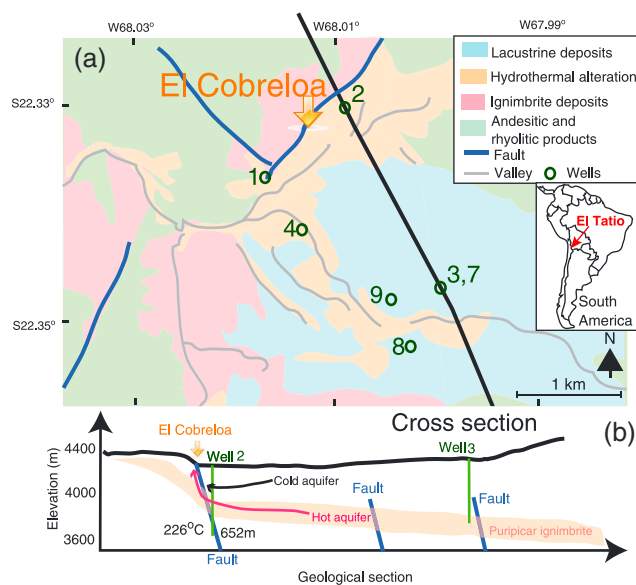


Figure 1. (a) Schematic geological map of El Tatio geothermal field. (b) Schematic cross section along the black line in Figure 1a. Figures 1a and 1b are based on Healy and Hochstein [1973], Cusicanqui et al. [1975], and Tassi et al. [2005, 2010]. The loci of valleys are traced from Google Earth.

These characteristics suggest that El Tatio geothermal water is a mixture of three water sources: hydrothermal, meteoric, and magmatic [Cusicanqui et al., 1975; Giggenbach, 1978; Cortecchi et al., 2005; Tassi et al., 2010]. The hypothesis of three water sources is consistent with the geothermal cross section suggested by Healy and Hochstein [1973].

Cusicanqui et al. [1975] measured Tritium content and concluded that the meteoric water recharged 15–20 km east of the geyser field and discharges with an age of 15–17 years [Cusicanqui et al., 1975; Giggenbach, 1978; Munoz and Hamza, 1993; Cortecchi et al., 2005]. Using this time and distance, and considering that precipitation occurs at altitudes of greater 5000 m, we infer a permeability of $\sim 10^{-11}$ m² for the aquifer.

3. Methods

We performed field experiments at El Tatio between 15 and 22 October 2012 and acquired data for El Cobreloa between 20 and 21 October. All dates and times are reported in local time. We conducted visual observations and made acoustic and temperature measurements.

For the visual observations, we used a digital video camera with a resolution of 1440 × 1080, recorded at 30 frames per seconds, and time was established with a GPS clock.

The acoustic and temperature data were acquired by a Hakusan LS-7000 data logger with a GPS clock. The acoustic measurements were collected at a sampling rate of 1000 Hz by a microphone (Primo MX5001) with a sensitivity of 5 mV Pa⁻¹ and a flat response in the frequency band of 1–5000 Hz. The microphone was located 3.5 m away from the vent in a northeasterly direction. Acoustic measurements can detect eruptions by increased amplitude of high-frequency sound. This method only works during the night time, since during the day strong winds generate too much noise.

We measured ground temperature at the surface with type K thermocouples located 5.5 m and 4 m away from the vent in easterly and northeasterly directions, respectively, at a sampling rate of 2 Hz. When an eruption causes a voluminous discharge of liquid water, the thermocouples located on the ground detect the flow of hot liquid water as an increase in temperature. The thermocouples are not fixed in place but simply lie on the ground. Hence, displacement of the thermocouples by flowing water or wind may cause small fluctuations in the measured temperature. The logger used for the temperature measurement does not have a sensor for reference temperature. Thus, the absolute value of the measured temperature is not reliable, and we only interpret the large and abrupt temperature changes.

4. Results

4.1. Visual Observations

Visual observations indicate that the El Cobreloa geyser has two distinct eruption styles: vigorous major eruptions and less energetic but more frequent minor eruptions.

Figure 2a and Movie S1 (in the supporting information) show the sequence of events at the geyser vent during a minor eruption. The numbers indicate the elapsed time after the beginning of the visual observation. At 52.7, 53.7, and 54.7 min, a splash of hot water is observed as white droplets. Such splashing occurs intermittently over an approximately 4 min time period.

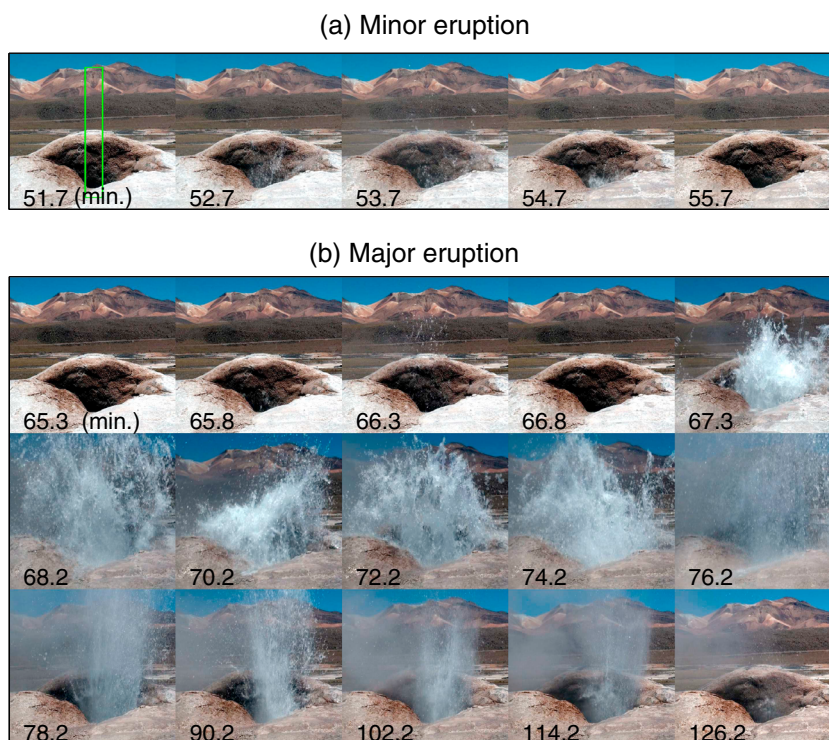


Figure 2. Visual observation of eruptions. (a) Minor eruption. The geyser splashes water droplets intermittently and the eruption ends within 4 min. The green box indicates the region shown in Figure 3. (b) Major eruption. The eruption begins with an eruption style similar to minor eruptions (65–67 min). At 67 min, a voluminous and liquid water-dominated eruption begins and finally ends with energetic steam discharge. In Figures 2a and 2b, numbers indicate the elapsed time after the beginning of visual observation. The field of view is approximately 1 m × 1 m.

Figure 2b and Movie S2 (supporting information) show the progression of a major eruption. Similar to minor eruptions, intermittent splashing of hot water is observed at 65.8 and 66.3 min. However, the eruption style transitions to a voluminous and liquid water-dominated eruption as shown in the photograph at 67.3 min. At 76.2 min the eruption style changes again to energetic steam discharge. The steam discharge continues for approximately 1 h without losing its vigor.

Figure 3a shows time evolution of the eruption sequence. The erupted water is shown as white vertical lines. The horizontal dark brown region shows the height range of the vent. Minor eruptions, labeled in pink, occur regularly. During the major eruption, the transition from the liquid water-dominated eruption to steam discharge is recognized by a change from whitish to grayish color, as observed in Figure 2b and Movie S2.

In order to remove the background landscape, we calculate the time derivative of Figure 3a shown in Figure 3b. Figure 3b only shows the water column. Figure 3c is the vertically averaged intensity of Figure 3b and is related to the water discharge velocity. The water discharge velocity of the minor eruptions increases with each subsequent eruption, as documented by the increasing intensity (Figure 3c). The inter-eruption quiet steam activity and wobble of the camera generate background noise. During major eruptions, the inside of the field of view is always filled with the water column, and the time difference becomes small despite the high discharge.

4.2. Ground Temperature Measurements

Figure 4 shows the measured ground temperature at the surface as a function of time. During the time period of the visual observations, the temperature rises abruptly. This time corresponds to the voluminous liquid-water eruption, when the flow of hot liquid water over the surface increased the ground temperature. We thus interpret the abrupt temperature rise as the beginning of a major eruption and voluminous liquid-water discharge. During 22 h of measurement, we documented five major eruptions.

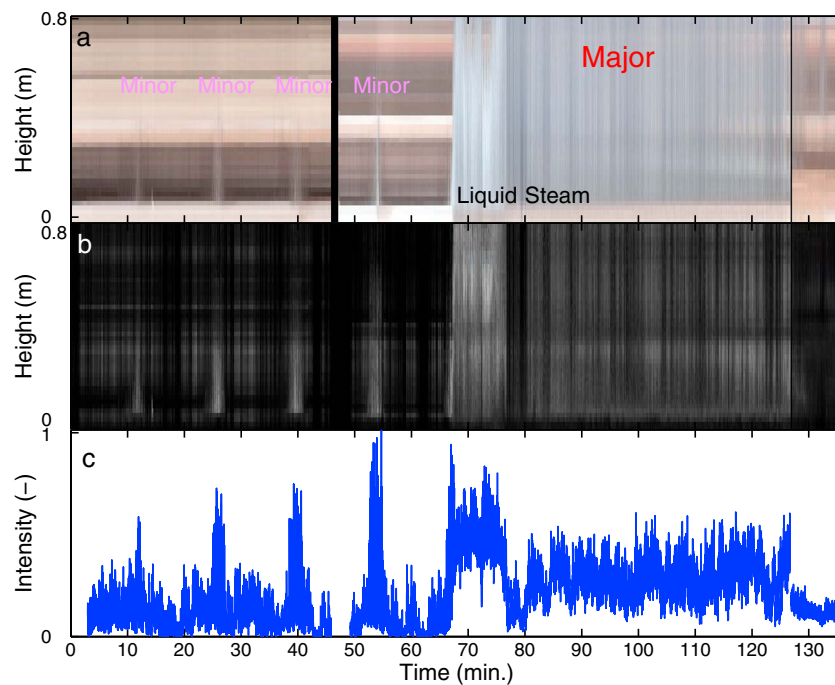


Figure 3. Time evolution of eruptions. (a) Time evolution of the water height by visual observations in the range indicated by the green box in Figure 2. Time increases to the right. White vertical lines indicate water (liquid and steam) eruptions. The black region indicates missing observations. In order to make this figure, we choose approximately same loci from videos with different angles of views. (b) Differences between the pictures shown in Figure 3a and those taken 0.5 s later. (c) Averaged intensity of Figure 3b as a function of time.

We calculated time intervals between major eruptions by selecting the time when the ground temperature exceeds 40°C. The calculated intervals are approximately 4 h and 40 min, indicating that major eruptions occur regularly, at least during the time period for which we have data.

4.3. Acoustic Measurements

Figure 5a shows temperature measurements during the time period indicated by the green arrow in Figure 4, during which it was not windy and acoustic measurements could detect eruptions. Figure 5b is a waveform of acoustic pressure with a frequency greater than 170 Hz, and Figure 5c shows the sound pressure level (amplitude) of Figure 5b. Here sound pressure level is defined by $SPL(dB) = 20 \log_{10}(\sqrt{p^2}/p_0)$, where p is the acoustic pressure, $p_0 = 2 \times 10^{-5}$ Pa, and the bar over p^2 means root-mean-square. Figure 5d is a spectrogram of acoustic measurements. Major eruptions occur twice during this time period. Figures 5b–5d

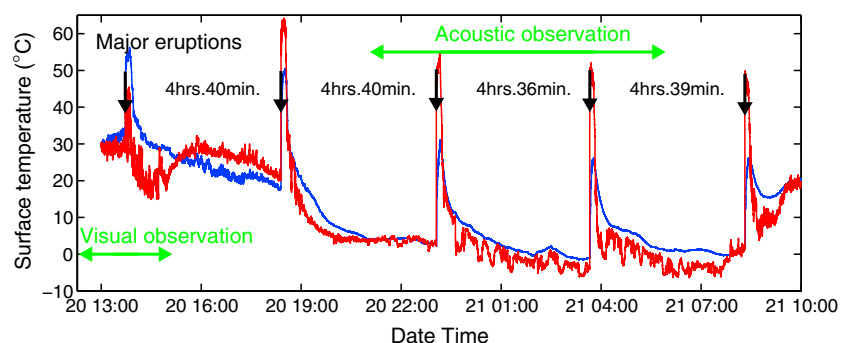


Figure 4. Measured ground temperatures at the surface. The blue and red curves are measured 5.5 m and 4 m away from the vent in easterly and northeasterly directions, respectively. The black arrows indicate the beginning of major eruptions determined by the time when the ground temperature exceeds 40°C. The time intervals between black arrows are denoted. The green arrows indicate the time periods shown in Figures 3 and 5. The time stamp on the horizontal axis is local time in Chile.

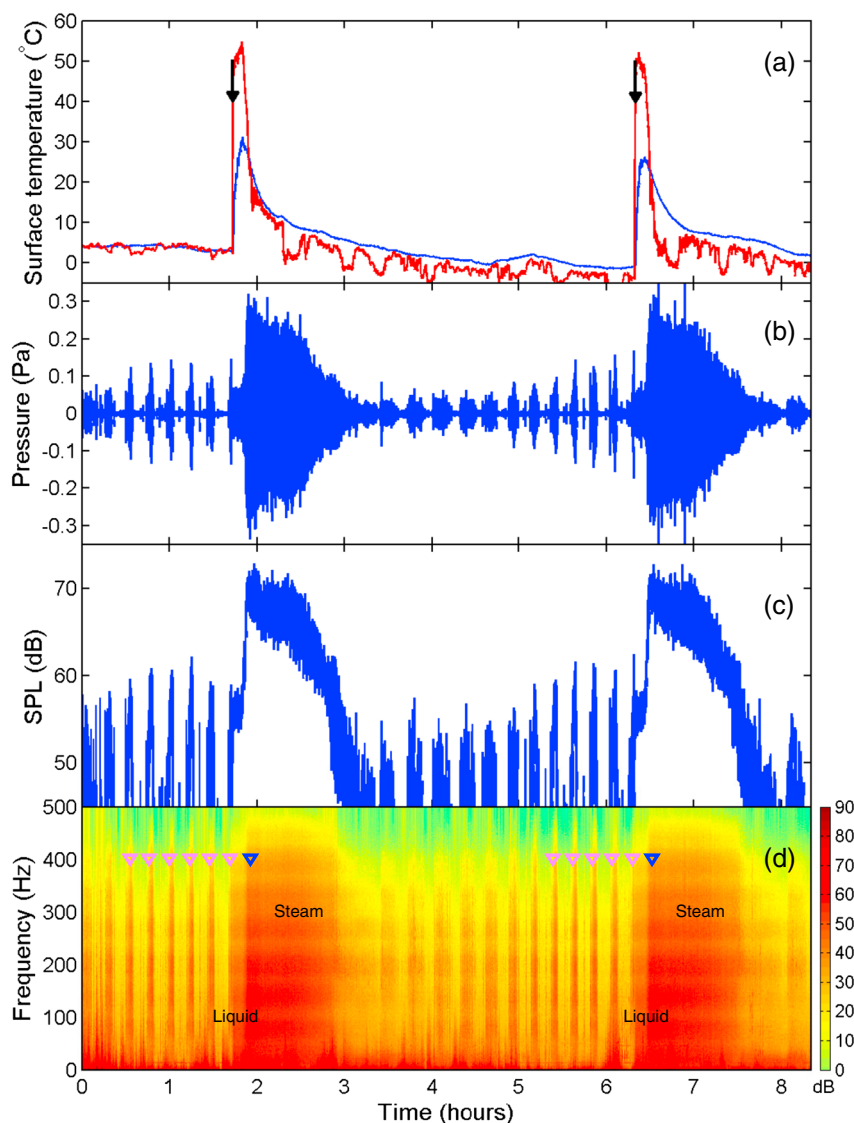


Figure 5. Minor eruptions identified by comparison between the temperature measurements and acoustic measurements. (a) Close-up view of ground temperature measurements for the time period shown by the green arrow in Figure 4. (b) A waveform of acoustic pressure measured by a microphone located 3.5 m away from the vent and filtered for frequencies higher than 170 Hz. (c) Sound pressure level of the waveform shown in Figure 5b. (d) Spectrogram of acoustic measurements denoted in sound pressure level. Reddish color indicates higher intensity. The pink triangles show the time when the intensity at the 400 Hz exceeds a threshold, indicating occurrences of minor eruptions and the beginning of major eruptions. The mean intervals of the pink triangles are 13 min and 43 s. The blue triangles indicate the mean interval after the beginning of major eruptions and are located close to the transition from the liquid water-dominated eruption to the steam discharge.

show that, when major eruptions occur, large amplitude sounds at high frequency are recorded. We thus attribute the high-frequency sound to the occurrence of eruptions.

High-surface temperatures persist for approximately 10 min (Figure 5a), a period similar to the duration of the liquid water-dominated eruption shown in Figure 2b. Approximately 10 min after the beginning of a major eruption, the amplitude and intensity of high-frequency components abruptly increase, documenting the transition from a liquid water-dominated eruption to a steam eruption (Figures 5b–5d).

Figures 5b–5d also show several spikes with high-frequency sound before major eruptions, indicating the occurrence of minor eruptions. Figures 5b and 5c show that the amplitude of the acoustic pressure and SPL signals tends to become larger with each subsequent minor eruption. This characteristic suggests that



Figure 6. Close-up view of the vent taken from above with the orientation direction of Figure 2. The red arrows show the ends of the vent.

minor eruptions become progressively more vigorous leading up to major eruptions, consistent with visual observations shown in Figure 3c. For the last minor eruption before the major eruption, the amplitude of the acoustic pressure signal decreases. This may be because larger volume liquid discharge does not increase the acoustic pressure. Note that all of the intermittent acoustic activity is not necessarily related with the liquid or steam discharge. We only observed four minor eruptions

before the major eruption through visual observation (Figure 2a). The acoustic activity with longer and small amplitude immediately after the major eruption may not produce liquid or steam discharge.

We calculate the eruption interval of possible minor eruptions and denote their occurrence by the pink triangles in Figure 5d. We chose the time when sound pressure level exceeds 20 dB (0.1 mPa) at 400 Hz measured 3.5 m away from the vent. This threshold is used for convenience and does not have any particular physical meaning. The calculated intervals vary from 13 min and 11 s to 14 min and 24 s, with a mean value of 13 min and 43 s. This measured interval is consistent with the visual observation in Figure 3. The minor eruptions also occur quite regularly.

The blue triangles indicate a time 13 min and 43 s (the interval between minor eruptions) after the beginning of the major eruption. The duration of liquid water-dominated eruption is slightly shorter than the time interval of minor eruptions.

4.4. Inferences of the Conduit Geometry

Although the conduit geometry is a key factor to understand geysering mechanisms, we do not have direct access inside the conduit. We here summarize the relevant constraints on conduit geometry.

Figure 6 shows a close-up view of the vent. The shape of the vent at the surface is more like a fissure than a cylinder. The red arrows indicate two ends of the vent. The length of the vent is approximately 0.2 m. The width of the vent becomes narrower with depth with an identifiable minimum of approximately 10^{-2} m. We cannot recognize whether the vent becomes wider or thinner with increasing depth. A gray wire for temperature measurements appears on the right of Figure 6, but we could not obtain data from this sensor because the instrument failed.

The volume of discharge provides a bound on the volume of the conduit and reservoir that store water beneath the surface. We here estimate the volume of discharge using visual observation instead of measuring the volume flux of stream flow generated by eruptions [e.g., *Karlstrom et al.*, 2013]. This is because, for minor eruptions, a very small volume of water is erupted and most of the water is absorbed by dry rocks. During the liquid water-dominated eruption, erupted water travels in all directions and it is not channelized into a small number of streams. During the steam-dominated eruption, most water ascends into the atmosphere as steam plumes.

For liquid water-dominated eruptions, we tracked erupted water droplets in the recorded video and obtained a discharge velocity of $\sim 1 \text{ m s}^{-1}$, consistent with an estimate based on the eruption height H (speed = $\sqrt{2gH}$). The liquid-dominated phase lasts for 10 min. Assuming that liquid water erupts out of the vent with a cross-sectional area of $0.2 \times 10^{-2} \text{ m}^2$ at a velocity of 1 m s^{-1} , the total discharge by the liquid-dominated phase becomes $1.2 \text{ m}^3 \sim 1.2 \text{ t}$.

During the steam eruption, both the tracking of water droplets and the eruption height imply an eruption speed of 10 m s^{-1} . Because the steam-dominated eruption continues approximately 1 h and the eruption of steam may be dominated by the phase change of hot liquid water to steam in a conduit, the volume of the erupted liquid water in the conduit is estimated as $7.2 \times 10^{-2} \text{ m}^3 \sim 72 \text{ kg}$, where we assume the ratio of the density of steam to liquid water is $\rho_g/\rho_l \sim 10^{-3}$. The estimated mass erupted by the steam-dominated eruption is less than 10% of that of the liquid-dominated phase.

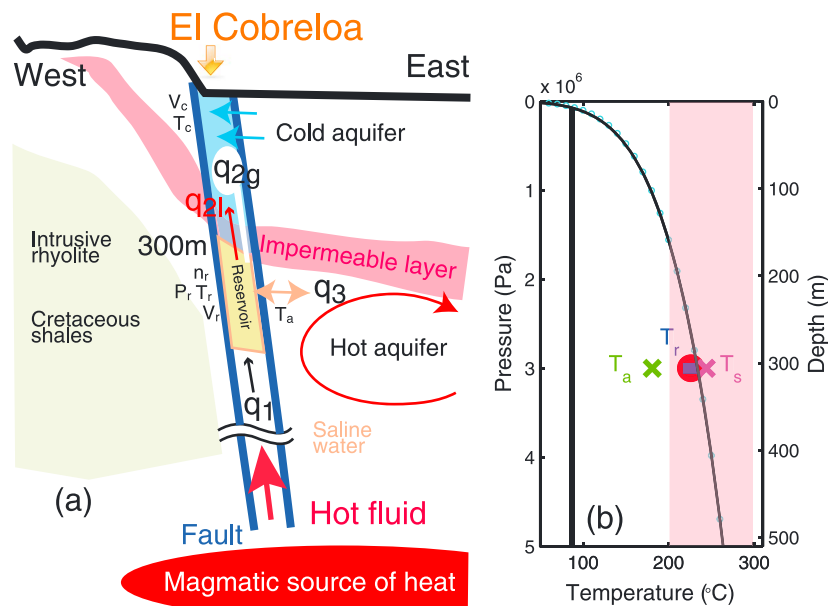


Figure 7. Possible conditions beneath the El Cobreloa. (a) Schematic diagram of the conduit beneath El Cobreloa modified from Healy and Hochstein [1973]. (b) The black curve shows a (P, T) boiling curve calculated by equation (15), assuming hydrostatic conditions with water density of 10^3 kg m^{-3} . Light blue dots indicate literature values. The thick vertical line indicates boiling temperature at the surface. The crosses denoted as T_s , T_a show the source and aquifer temperature assumed in our model. The horizontal blue bar T_r indicates the calculated temperature range of the reservoir in our model. The red dot indicates the highest temperature measured in well 2. The pink region indicates the possible temperature range of the high chloride water, including the measured temperature range and geochemically estimated values [Cusicanqui et al., 1975; Tassi et al., 2005].

For minor eruptions, we do not estimate the discharged volume. This is because visual observations in Figure 2a suggest that the erupted volume is quite small compared to major eruptions. In addition, intermittent splashing of water droplets observed in Figure 2a suggests that the minor eruption is rather gaseous. We do not know the liquid/steam ratio in the erupted water and cannot use the same method used for major eruptions. We thus conclude that the volume of the liquid water stored in the conduit and reservoir before the eruption is 10^0 m^3 .

5. Discussion

We now use our surface observations, along with geological and geochemical constraints, to develop a conceptual model, and then an idealized thermal and mechanical model, for the El Cobreloa geyser. To begin, we highlight key observations and inferences that a model should explain.

1. Major eruptions occur regularly with an interval of approximately 4 h and 40 min.
2. Major eruptions begin with a liquid water-dominated eruption and change to a steam eruption.
3. Minor eruptions occur regularly with an interval of approximately 14 min.
4. Minor eruptions involve the bursting of many bubbles over a 4 min period.
5. Minor eruptions discharge water, indicating that the water level in the conduit does not vary much between minor and liquid water-dominated major eruptions.
6. Minor eruptions become progressively more vigorous leading up to major eruptions, implying that minor eruptions successively change conditions in the conduit.

5.1. An Estimate of Areal Dimensions of the Conduit

As we have previously discussed in section 2, exploration and production wells drilled in the early 1970s, as well as recent geochemical measurements of discharge, provide some constraints on subsurface fluids, lithology, and temperature [Healy and Hochstein, 1973; Cusicanqui et al., 1975; Tassi et al., 2010]. The closest well to El Cobreloa is well 2 (Figure 1), whose depth was 652 m and maximum measured temperature was 226°C [Cusicanqui et al., 1975].

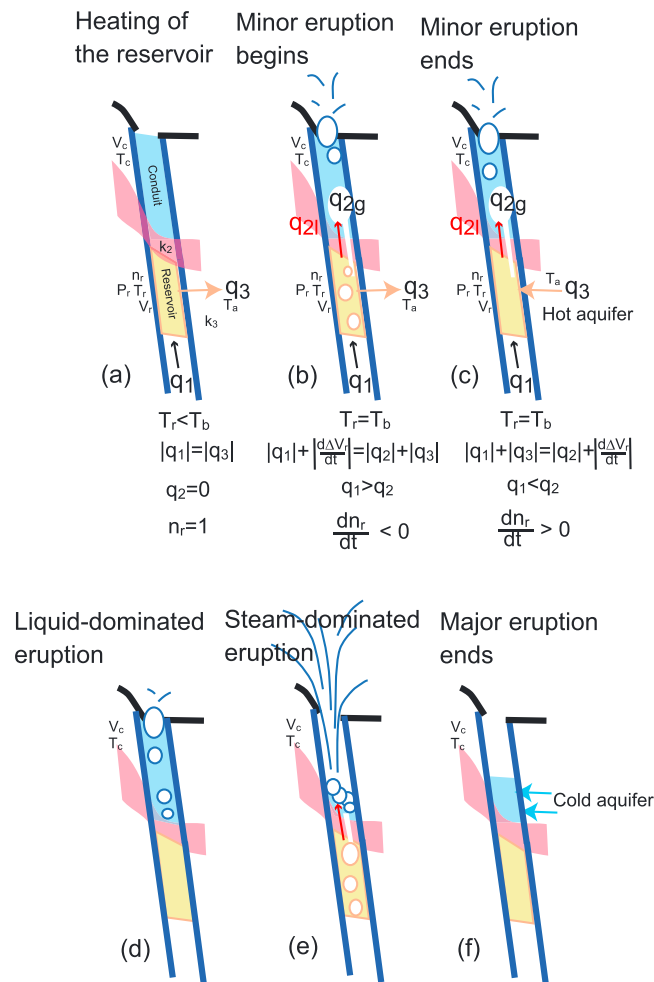


Figure 8. (a–f) Schematic diagrams of the sequence of geysering.

within the fault zone is assumed to be higher than that of the surrounding rocks, so that the fault serves as a conduit for vertical flow. The transport of fluids through the fault is governed by its equivalent permeability, and we consider the case where the fault zone permeability is lowest at the depth of the impermeable layer. Ascending steam in the conduit is trapped below this depth to mix with, and heat, the surrounding aquifer. This region behaves as a reservoir. We thus locate the reservoir approximately 300 m below the surface, based on Figure 1. This depth is much greater than the depth of reservoirs inferred at other geysers [e.g., Rudolph et al., 2012; Vandemeulebrouck et al., 2013].

As we have estimated in section 4.4, the volume of the preeruption liquid water within the conduit is approximately 1 m^3 . If the entire conduit above the reservoir, with a height of 300 m, is evacuated during the eruption, the mean cross-sectional open area of the conduit becomes approximately twice that of the vent, $0.2 \times 10^{-2} \text{ m}^2$. We thus assume that the mean cross-sectional area of the conduit is $0.4 \times 10^{-2} \text{ m}^2$, which is the void space in the void and rock mixture.

Using this geometry, the thickness of erupted water during the steam-dominated eruption becomes $0.072 \text{ m}^3 / (4 \times 10^{-3} \text{ m}^2) \sim 18 \text{ m}$. During the liquid water-dominated eruption with a surface eruption rate of 1 m s^{-1} , the unloading rate of the liquid water becomes $1/2 \sim 300 \text{ m} / 10 \text{ min} \sim 0.5 \text{ m s}^{-1}$. On the other hand, the steam-dominated eruption, which continues approximately 1 h at an eruption velocity of 10 m s^{-1} , descends at $10/2 \cdot \rho_g / \rho_l \sim 5 \times 10^{-3} \text{ m s}^{-1}$.

All the numbers in the above and subsequent discussions are based on a reservoir at 300 m, but this depth can be changed and all derived quantities would change accordingly. At the depth of 300 m, hydrostatic pressure is approximately $3 \times 10^6 \text{ Pa}$, and the boiling temperature is approximately 234°C .

Three observations are pertinent. First, waters with high chloride concentrations discharged from well 2 on initial opening. In addition, a saturated brine with density of 1200 kg m^{-3} was found at a depth below approximately 600 m. Steam separation may generate the high chloride water [Cusicanqui et al., 1975; Giggerbach, 1978]. Second, the high $^3\text{He}/^4\text{He}$ ratio and gas and major ion chemistry in the water from El Tatio suggest magmatic input and high temperature of $\sim 270^\circ\text{C}$ [Urzua et al., 2002; Cortecci et al., 2005; Tassi et al., 2005, 2010]. Third, regional aquifers transport hot and cold water laterally [Healy and Hochstein, 1973].

Based on these observations and the geological cross section provided by Healy and Hochstein [1973] and shown in Figure 1b, we consider the subsurface geometry and flow pathways shown in Figure 7a. There are two aquifers separated by an impermeable layer [Healy and Hochstein, 1973], with the deeper aquifer having a higher temperature. These characteristics are consistent with the three water sources suggested by geochemical analysis, i.e., hydrothermal, meteoric, and magmatic [Tassi et al., 2005]. A fault intersects the impermeable layer. The vertical permeability

5.2. Conceptual Model

We here assume the geometry shown in Figure 7 and consider how it explains the two eruption styles observed in El Cobreloa. Figure 8 illustrates schematically the various stages in the eruption. We attribute minor and major eruptions to boiling in the reservoir and conduit, respectively. In Figure 8, we consider the following situation.

1. The “reservoir,” at the base of the geyser conduit, deeper than 300 m, is filled with hot and dense chloride-rich water. From Figure 1, we infer that the height of the reservoir is approximately 100 m. Steam is supplied from below to heat the water inside the reservoir, with constant mass flux $q_{1\text{mass}}$ at a temperature T_s . This boundary condition implies a constant heat and mass flux at depth, consistent with other models [i.e., *Ingebritsen et al.*, 2006; *Shteinberg et al.*, 2013]. The flux from below may originate from some combination of gas exsolved from magmas cooling at depth and hydrothermal fluids. If the magma cools at a constant rate, gas exsolution is approximately constant, also leading to a constant mass flux. Convection of hydrothermal fluid at a constant velocity with steady steam-liquid ratio will also generate a constant mass flux. Over the timescale of many geyser eruptions, the deeper processes supplying fluids are unlikely to change.
2. Permeable flow through a layer of low permeability that separates the reservoir from overlying parts of the conduit. The thickness of the low permeability layer is immaterial. This is because, in permeable flow, the flux q_2 is determined by the pressure gradient which is calculated by the product of density difference and gravitational acceleration, and is independent of the thickness, that is, $q_2 \propto dP/dz \propto (\rho_l - \rho_g)g$, where P is pressure, z is the vertical coordinate, and g is gravitational acceleration.
3. Negligible flow resistance through that overlying conduit except at the vent which may act to throttle flow during eruptions. It is not obvious whether the conduit is a crack or a conventional porous medium; in our model, the difference between two assumptions is not significant, since the formulation for channel flow and permeable flow is basically the same.
4. We assume that the cross-sectional area of the void space in the reservoir or conduit is the same and twice of the vent area $S = 4 \times 10^{-3} \text{ m}^2$.
5. Flow between the reservoir and an adjacent hot aquifer occurs at a rate sufficient to balance other reservoir fluxes. Since the reservoir has a finite volume and chloride-rich water is more dense, some amount of liquid water flows into the surrounding aquifer, q_3 (Figure 8a). In our model, we calculate q_3 passively and do not solve Darcy’s equation. This is because, in order to calculate q_3 based on Darcy’s law, we would need to assume the contacting area between the hot aquifer and the reservoir, which is unknown. This approach implies that water flows into and out of the deep aquifer with relative ease compared to the flow between the reservoir and conduit. This is expected both because of the high permeability of regional aquifers, $k_3 = 10^{-11} \text{ m}^2$, and the possibly large surface area over which q_3 occurs, likely much greater than the cross-sectional area of the conduit. Since we assume a constant mass and heat flux from the bottom to the reservoir, once the inside of the reservoir boils, the volume flux increases. As a result, the flux from the reservoir to the aquifer q_3 increases, and pressure inside the reservoir will also increase. We can estimate the lateral pressure gradient by assuming permeable flow through the side-surface area of the reservoir of S_3 , $q_1 \sim q_3 = S_3 k_3 / \mu_1 \cdot dP/dx$, where μ_1 is viscosity of water and x is the horizontal coordinate. In our calculation, $dP/dx \ll (\rho_l - \rho_g)g$ for both temperatures at, and below, boiling temperatures in the reservoir when $q_3 > 0$. We thus find that pressurization inside the reservoir by boiling does not affect the vertical mass and heat transfer provided by buoyancy of steam.
6. When the temperature inside the reservoir exceeds the boiling point, buoyant steam is generated. The buoyancy generates an upward flux q_2 . The flux from the reservoir to the conduit may generate gas slugs in the conduit that culminate in minor eruptions (Figure 8b). Though there may be variations in temperature within the reservoir, we assume that discharge q_2 begins when the shallowest part of the reservoir exceeds the boiling temperature.
7. If the upward flux exceeds the supply from below, $q_2 > q_1$, the liquid water in the surrounding hot aquifer will flow back into the reservoir, i.e., the flow direction of q_3 reverses. When the water in the hot aquifer is colder than that in the reservoir, the water temperature decreases, steam disappears, and the minor eruption ends (Figure 8c). The steam supply from the bottom continues, however, and the processes leading to minor eruptions are repeated (Figure 8a).
8. The flux from the reservoir to the conduit, q_2 , heats water in the conduit by condensing part of the supplied steam. In particular, immediately after the major eruption, the water in the conduit is cool and more

- gas bubbles collapse to generate acoustic activity. In Figure 5b, the amplitude of acoustic activity is small after the major eruption and progressively becomes larger.
9. Water inside the conduit never flows into the reservoir, though the water in the reservoir flows into conduit. If the heated water in the conduit were to flow back into the reservoir, the time interval between minor eruptions would decrease over time.
 10. We assume that the timescale of heat supply determines the interval between eruptions, which explains the constant interval of minor eruptions, though there may exist a case in which mass supply determines the intervals between eruptions [Ingebritsen and Rojstaczer, 1993, 1996; Rojstaczer et al., 2003].
 11. Major eruptions occur when water in the upper conduit is warm enough that removal of cold shallow liquid water by small eruptions allows water deeper in the conduit to reach the boiling temperature (Figure 8d). Then, progressive and continued eruption propagates downward and erupts most of water in the conduit, at which point the eruption becomes steam dominated (Figure 8e). The steam discharge may be regulated at the vent and hence allow high pressures to persist during the eruption [Kieffer, 1989; Karlstrom et al., 2013], preventing liquid flow from surrounding aquifers from quenching the eruption. Boiling of hot water from the reservoir within the conduit maintains the steam eruption. Eventually, all water in the conduit boils, and liquid water from the cold aquifer flows into the conduit to end the major eruption.
 12. After large eruptions, the conduit above the reservoir is immediately flooded by liquid from a surrounding colder aquifer, and then little additional cold water flows into the conduit until the end of the next major eruption (Figure 8f). This is because there is little water discharged during minor eruptions, suggesting that the water level in the conduit remains high, balancing the pressure in the surrounding cold aquifer.
 13. Repeated boiling increases the concentration of chloride-rich water in the reservoir by removing water as steam (Figure 8b). The low chloride concentration in steam supplied from below, q_1 , may dilute the reservoir water to allow the concentration to reach steady state, while continuous boiling at depth (q_1) generates more concentrated brine as is observed in well 2. Transport of chloride-rich water into the conduit during minor eruptions allows some of it to be evacuated during the liquid water-dominated stage of the major eruptions (Figure 8d).

5.3. Balance Between Three Volume Fluxes

We now apply relationships for conservation of mass and energy to the conceptual model described in section 5.2 and illustrated in Figure 8. We approximated the momentum equation by Darcy's law and substitute it into the mass conservation equation [Ingebritsen et al., 2006]. In doing so, we will necessarily need to make many assumptions and introduce several idealizations. The objective is not to capture all the features of El Cobreloa's plumbing, which are unknown in detail, but rather to see whether the various ideas illustrated in the conceptual model are in fact possible. We focus only the feedbacks that lead to periodic minor eruptions. Notation is summarized in Table 1.

We assume that the mass flux of hot geothermal fluid to the reservoir $q_{1\text{mass}}$ is constant, (section 5.2, item 1: Steinberg et al. [1981]). The volume flux q_1 depends on whether the reservoir temperature T_r exceeds the boiling temperature T_b , that is (section 5.2, item 5)

$$q_1 = \frac{q_{1\text{mass}}}{\rho_g}, \text{ for } T_r \geq T_b \quad (1)$$

$$q_1 = \frac{q_{1\text{mass}}}{\rho_l}, \text{ for } T_r < T_b, \quad (2)$$

where $\rho_g = 13 \text{ kg m}^{-3}$ and $\rho_l = 820 \text{ kg m}^{-3}$ are the steam and liquid water density at the reservoir, respectively. For simplicity, we assume the density of the steam is constant. Given that the reservoir is located at 300 m depth, where the hydrostatic pressure is high, $P_r \sim 3 \text{ MPa}$, perturbations to the static pressure inside the reservoir are relatively small. For instance, the perturbation of static pressure generated by a long slug with a length of 1 m is 10^4 Pa , which generates pressure and density perturbations less than 1%.

Buoyancy drives fluid from the reservoir to the conduit, with volume flux q_2 , (section 5.2, item 6). The vertical buoyancy with a volumetric liquid fraction of n_r is given by $(\rho_l - \rho_m)g = (\rho_l - \rho_g)(1 - n_r)g$, where $\rho_m = \rho_l n_r + \rho_g(1 - n_r)$ is the mean density in the reservoir. Thermal expansion is neglected because

Table 1. Notations

Parameter	Values	Unit	Description
n_r	-	-	Volume fraction of liquid water in the reservoir
P_r	3×10^6	Pa	Pressure at the reservoir
C_p	4700	$\text{J kg}^{-1} \text{K}^{-1}$	Specific heat for liquid water
C_{pst}	2050	$\text{J kg}^{-1} \text{K}^{-1}$	Specific heat for steam
L	2.25×10^6	J kg^{-3}	Latent heat
g	9.8	m s^{-2}	Gravitational acceleration
k_2	4.5×10^{-9}	m^2	Permeability for outlet of the reservoir
T_r	-	$^{\circ}\text{C}$	Reservoir temperature
T_b	234	$^{\circ}\text{C}$	Boiling temperature at P_r
T_s	244	$^{\circ}\text{C}$	Source temperature
T_a	181	$^{\circ}\text{C}$	Aquifer temperature
-	87	$^{\circ}\text{C}$	Boiling temperature at the surface
h_r	-	J kg^{-1}	Enthalpy per unit mass in the reservoir
h_l	1.1×10^6	J kg^{-1}	Enthalpy per unit mass beginning of boiling $C_p T_b$
h_g	3.3×10^6	J kg^{-1}	Enthalpy per unit mass end of boiling $C_p T_b + L$
h_s	3.4×10^6	J kg^{-1}	Enthalpy per unit mass of source steam
q	-	m^3	Volume flux of water
$q_{1\text{mass}}$	1.5×10^{-2}	kg s^{-1}	Mass flux from the source
S	4×10^{-3}	m^2	Cross-sectional area of the void space of conduit
D	-	m	Typical thickness of the conduit
U_g	-	m s^{-1}	The speed of the steam
f	0.07	-	Friction factor
V_r	0.32	m^3	Volume of the reservoir
V_c	1.2	m^3	Volume of the conduit
M_c	1200	kg	Water mass in the conduit
μ_l	10^{-3}	Pa·s	Viscosity of liquid water
μ_g	10^{-5}	Pa·s	Viscosity of steam
ρ_l	820	kg m^{-3}	Density of liquid water at the reservoir
ρ_g	13	kg m^{-3}	Density of steam at the reservoir

Subscripts	
c	Conduit
r	Reservoir
s	Source
l	Liquid
g	Gas (Steam)
1	Between source and reservoir
2	Between reservoir and conduit
3	Between reservoir and aquifer

bubbles have a much larger effect on buoyancy. The volume flux q_2 is calculated by permeable flow law (section 5.2, item 2),

$$q_2 = q_{2g} + q_{2l} \quad (3)$$

$$q_{2g} = \left[\frac{k_2 k_{rg} (1 - n_r)}{\mu_g} \right] (\rho_l - \rho_g) (1 - n_r) g S, \quad (4)$$

$$q_{2l} = \left[\frac{k_2 k_{rl} n_r}{\mu_l} \right] (\rho_l - \rho_g) (1 - n_r) g S, \quad (5)$$

where $\mu_g = 10^{-5}$ Pa s and $\mu_l = 10^{-3}$ Pa s are the steam and liquid viscosity, respectively, S is cross-sectional area of void space of the conduit (section 5.2, item 4), k_2 is the permeability between the reservoir and conduit, and k_{rg} and k_{rl} are relative permeabilities for gas and liquid phases. Permeability depends on liquid saturation n_r [e.g., Corey, 1957], and measured relative permeabilities k_{rg} and k_{rl} usually satisfy the condition that $k_{rg} + k_{rl} < 1$. For simplicity, we adopt a linear relationship [e.g., Ingebritsen *et al.*, 2006], with

$$k_{rl} = (n_r - 0.3)/0.7, \quad k_{rg} = (1 - n_r)/0.7, \quad \text{for } n_r > 0.3 \quad (6)$$

$$k_{rl} = 0, \quad k_{rg} = 1, \quad \text{for } n_r < 0.3. \quad (7)$$

The flow of liquid water into and out of the deep aquifer, q_3 , would be governed by a groundwater flow equation that couples conservation of mass and Darcy's law within the aquifer. As this introduces many unknowns, we obtain q_3 by the balance of volume fluxes in the reservoir (section 5.2, item 5),

$$q_3 = q_1 - q_2 + \frac{d\Delta V_r}{dt}, \quad (8)$$

where a positive sign indicates that fluid flows out of the reservoir. The flow direction of q_3 can reverse (section 5.2, item 7). In equation (8), ΔV_r is the volume change of water caused by phase changes produced by enthalpy changes,

$$\Delta V_r = \frac{M_r x_f}{\rho_l} + \frac{M_r(1-x_f)}{\rho_g} - V_r, \quad (9)$$

where V_r is the volume of the reservoir and x_f is the mass fraction of liquid water in the reservoir,

$$x_f = \left[\frac{\rho_g}{\rho_l} \left(\frac{1}{n_r} - 1 \right) + 1 \right]^{-1}. \quad (10)$$

In equation (9), mass in the reservoir is obtained by

$$\frac{dM_r}{dt} = q_{1\text{mass}} - q_{2\text{mass}} - q_{3\text{mass}}, \quad (11)$$

where we assume that q_3 is liquid water.

The enthalpy change within the reservoir per unit mass, h_r , is given by

$$\frac{d(h_r \rho_m V_r)}{dt} = q_{1\text{mass}} h_s - q_{2g} \rho_g h_g - q_{2l} \rho_l h_l - q_{3l} \rho_l h_l, \text{ for } q_3 > 0 \quad (12)$$

$$\frac{d(h_r \rho_m V_r)}{dt} = q_{1\text{mass}} h_s - q_{2g} \rho_g h_g - q_{2l} \rho_l h_l - q_{3l} \rho_l h_a, \text{ for } q_3 < 0, \quad (13)$$

where $h_g = C_p T_b + L$ and $h_l = C_p T_b$ are the enthalpies of gas and liquid per unit mass at boiling temperature T_b , respectively, $h_a = C_p T_a$ is the enthalpy of liquid water per unit mass in the aquifer at temperature T_a , $h_s = C_p T_b + L + C_{\text{pst}}(T_s - T_b)$ is the enthalpy of steam supplied from below the reservoir at temperature T_s , where $L = 2.25 \times 10^6 \text{ J kg}^{-1}$ is latent heat, $C_p = 4700 \text{ J kg}^{-1} \text{ K}^{-1}$, and $C_{\text{pst}} = 2050 \text{ J kg}^{-1} \text{ K}^{-1}$ is specific heat of liquid water and steam, respectively.

The liquid water fraction can then be computed

$$n_r = \frac{\rho_g (h_r - h_g)}{\rho_l h_l - \rho_g h_g - (\rho_l - \rho_g) h_r}. \quad (14)$$

We approximate the boiling curve by

$$T_b = \frac{b_2}{b_1 - \log P}, \quad (15)$$

where $b_1 = 24.2$ and $b_2 = 4.7 \times 10^3$. Calculated T_b shown by the black curve in Figure 7b fits equation-of-state data well [Hayashi et al., 2013].

5.4. Possible Parameter Values and Ranges

The model formulation in the previous section involves several parameters, in particular permeabilities, fluxes, and temperatures. Here we use observations to provide estimates of reasonable values. Based on drilling, we assume a reservoir depth of 300 m and take the cross section of the void space of the conduit S to be constant, even though downhole measurements elsewhere clearly show that this is not the case [Hutchinson et al., 1997].

5.4.1. Permeability Between the Reservoir and the Conduit, k_2

Assuming that the steam-dominated eruption represents boiling of water inside the conduit derived from the boiling reservoir, we can estimate the permeability k_2 . During the 60 min of the steam-dominated eruption, the equivalent of 18 m of liquid water is erupted, thus $q_{2l}/S = 5 \times 10^{-3} \text{ m s}^{-1}$. Assuming $n_r \sim 0.5$ in equation (5), we obtain $k_2 = 9 \times 10^{-9} \text{ m}^2$. The permeability between the conduit and reservoir should be larger than the permeability of the surrounding aquifer $k_3 \sim 10^{-11} \text{ m}^2$ (section 2). We thus consider an estimated permeability of k_2 with orders of magnitude of $10^{-9} - 10^{-8} \text{ m}^2$ to be reasonable. In order to explain details of eruptions in the next section, we use a similar $k_2 = 4.5 \times 10^{-9} \text{ m}^2$. This value is similar to the value used in Ingebritsen and Rojstaczer [1993, 1996].

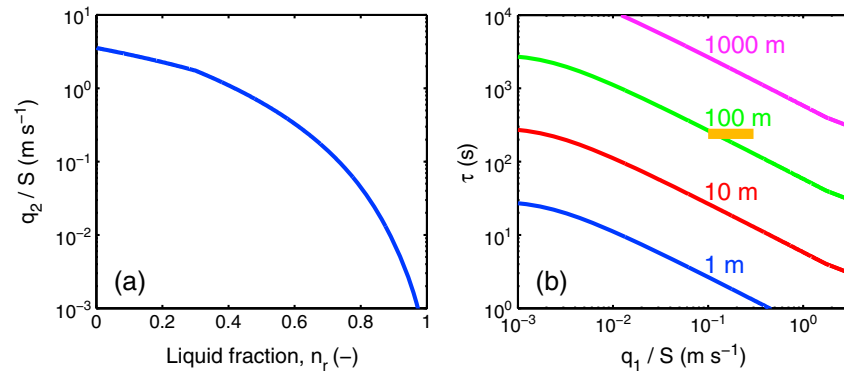


Figure 9. (a) Calculated flux from the reservoir to the conduit by equations (3)–(5) as a function of liquid fraction in the reservoir n_r , assuming $k_2 = 4.5 \times 10^{-9} \text{ m}^2$. (b) Time duration for the minor eruption estimated by equation (16) for varying length of reservoir V_r/S . The horizontal orange bar indicates the time duration of 4 min and our preferred q_1/S .

5.4.2. Flux From the Source, $q_{1\text{mass}}$

Using this permeability, we calculate the flux from the reservoir to the conduit, q_2/S , by equations (3)–(5), shown in Figure 9a as a function of liquid fraction in the reservoir. The maximum estimate of the flux is $q_2/S = 4 \text{ m s}^{-1}$ for $n_r = 0$, indicating that the flux from the source $q_1/S < 4 \text{ m s}^{-1}$. If $q_1/S > 4 \text{ m s}^{-1}$, the reservoir will always be above the boiling temperature and we should expect fumaroles rather than geysers.

From the duration of the minor eruptions, we can constrain q_1/S more quantitatively. If we assume that the gas fraction inside reservoir increases linearly over time during the minor eruption, the gas fraction at time τ is obtained from

$$\tau \sim \frac{V_r(1 - n_r)}{q_1}, \quad (16)$$

where q_1 is a function of the reservoir temperature and $T_r = T_b$. When the flux from the reservoir to the conduit exceeds that from below ($q_2 > q_1$), boiling inside the reservoir ends. The profile of q_2 is defined by equations (3)–(5) and is plotted in Figure 9a. Substituting $q_1 = q_2$ into equations (3)–(5) and (16) to remove n_r , we obtain the duration of minor eruptions produced by boiling inside the reservoir as a function of the vertical dimension of the reservoir (Figure 9b).

From the thickness of the hot aquifer in *Healy and Hochstein* [1973], we assume that the vertical height of the reservoir is, to order of magnitude, 10^2 m . The flux from the source to explain the 4 min duration of minor eruptions is then $q_1(T_r = T_b)/S \sim 10^{-1} \text{ m s}^{-1}$. Later we use a similar $q_1(T_r = T_b)/S = 0.3 \text{ m s}^{-1}$ to explain details of the eruptions as shown by the horizontal orange bar in Figure 9b. Thus, the mass flux from the source is estimated to be $q_{1\text{mass}} = q_1(T_r = T_b) \cdot \rho_g = 1.5 \times 10^{-2} \text{ kg s}^{-1}$.

5.4.3. Aquifer Temperature, T_a

Using the interval between the end and resumption of minor eruptions of 10 min, which we attribute to the time required to heat the reservoir water to the boiling temperature (section 5.2, item 10), we can estimate the temperature of the surrounding aquifer. When the liquid water flows into the reservoir from the aquifer, the reservoir temperature will approach the aquifer temperature T_a . In order to initiate a new minor eruption, the reservoir temperature must rise to T_b . Using this timescale, we obtain a relationship between q_1 , T_a , and T_s . Before boiling occurs, the temperature increase in the reservoir is

$$\frac{dT}{dt} = \frac{q_{1\text{mass}}(h_s - h_r)}{\rho_l V_r C_p}. \quad (17)$$

Using the initial condition $T = T_a$ at $t = 0$ and integrating, we obtain

$$T - T_a = \left[\frac{h_s - h_a}{C_p} \right] \left[1 - \exp \left(-\frac{q_{1\text{mass}} t}{\rho_l V_r} \right) \right]. \quad (18)$$

Figure 10 shows the relationship between aquifer temperature T_a , $q_1 = q_{1\text{mass}}/\rho_g$ and V_r required to produce 10 min eruption intervals. Here the boiling temperature of the reservoir is $T_b = 234^\circ\text{C}$. If the aquifer temperature is between 87 and 217°C , which spans the range between the boiling temperature at local

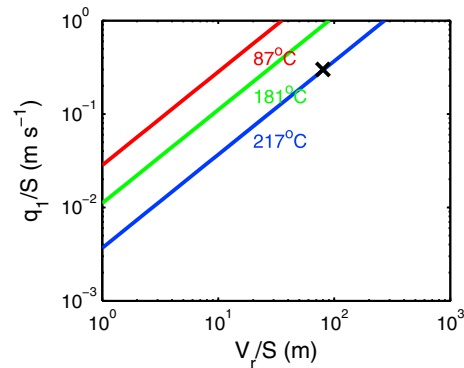


Figure 10. Relation between the length of the reservoir V_r/S and source flux velocity q_1/S , where $T_r = T_b$ and we assume constant cross-sectional area $S = 0.01 \times 0.2 \times 2 \text{ m}^2$, twice that of the vent. The colors indicate results for different aquifer temperatures T_a in equation (18). The boiling temperature of the reservoir is $T_b = 234^\circ\text{C}$. The black cross is the condition used in our preferred model.

atmospheric pressure and 17°C below the boiling temperature of the reservoir, q_1/S and V_r/S have values between the red and blue lines. Since we are assuming $V_r/S \sim 10^2 \text{ m}$ and $q_1(T_r = T_b)/S = 0.3 \text{ m s}^{-1}$, the lowest temperature inside the reservoir is estimated as 217°C . In reality, when the liquid in the surrounding aquifer flows into the reservoir, there remains a finite volume of reservoir water, so that the reservoir temperature does not decrease to the aquifer temperature. In our simulation, we assumed an aquifer temperature of $T_a = 181^\circ\text{C}$, and obtained the lowest reservoir temperature of 217°C . Here we first estimate the possible range of T_a using Figure 10 and obtain detailed numbers from numerical calculations that explain the minor eruption intervals.

Although we do not have a method for quantitatively constraining T_s , the estimated temperature at (even greater) depth is $\sim 270^\circ\text{C}$ [Tassi et al., 2010], exceeding the reservoir's boiling temperature. Here we expect that the temperature of source fluid is closer to the reservoir temperature than that of the aquifer, i.e., $T_s - T_b < T_b - T_a$.

This is because the maximum flux from the reservoir to the upper conduit is $q_1 \sim q_2$. In this limit, the flow from the aquifer to the reservoir $q_3 = q_1 - q_2$ is small; in order to efficiently cool the reservoir and suppress boiling, $T_s - T_b \ll T_b - T_a$. Regardless, the effect of T_s on heating is limited, since $L \gg C_{\text{pst}}(T_s - T_b)$. The source temperature does not affect the relationship between q_1 and V_r , significantly. We thus consider $T_s - T_b = 10^\circ\text{C}$ to be a reasonable assumption. Here q_1 is a result of boiling at deeper depth, and the geothermometry suggests that the source temperature is 270°C [Tassi et al., 2010]. Our estimate of $T_s = 244^\circ\text{C}$ is close to and less than 270°C . Again, this is a reasonable assumption.

5.4.4. Steam Flow Velocity, U_g

Finally, we consider the conditions necessary to sustain the steam-dominated component of the major eruptions. In order to continue discharging steam, conditions inside the conduit must be maintained close to or higher than hydrostatic pressure, to prevent liquid water from the shallow, colder aquifer from entering the conduit.

We infer that frictional flow or choked flow at the vent maintains the high pressure inside the conduit (items 3 and 11 in section 5.2). If the steam discharge from the vent is slow enough to be compensated by the supply of steam from boiling, the pressure inside the conduit remains constant. We have estimated that the cross-sectional area of the vent is smaller than that of the conduit. If the cross-sectional area of the vent is a local minimum, this geometry becomes a geologic nozzle [Kieffer, 1989]. When flows both inside and outside the conduit are subsonic, the flow velocity inside the conduit accelerates at shallower depth and becomes maximum at the vent. When the flow outside the conduit is supersonic, the flow velocity at the vent is limited to the sound velocity. This is because, for steady flows, conservation of mass requires

$$\rho_g U_g S = \text{constant}, \quad (19)$$

where U_g is the speed of the steam.

In Figure 11a, we estimate the steam density (blue line) required to balance hydrostatic pressure at the boiling temperature (red curve). Since steam becomes less dense at shallower depth, when the cross-sectional area of the conduit is constant, the flow velocity accelerates at shallower depth. In Figure 11b, we calculate the black curve by assuming that the cross-sectional area of the conduit beneath the vent is twice that of the vent, so that the flow at the top of the conduit is half of the observed vent velocity, 5 m s^{-1} .

When the flow velocity reaches its maximum at the vent, this speed may be regulated by friction, which is calculated by the balance with the dynamic pressure gradient

$$\frac{dP}{dz} = \frac{f \rho_g U_g^2}{2D}, \quad (20)$$

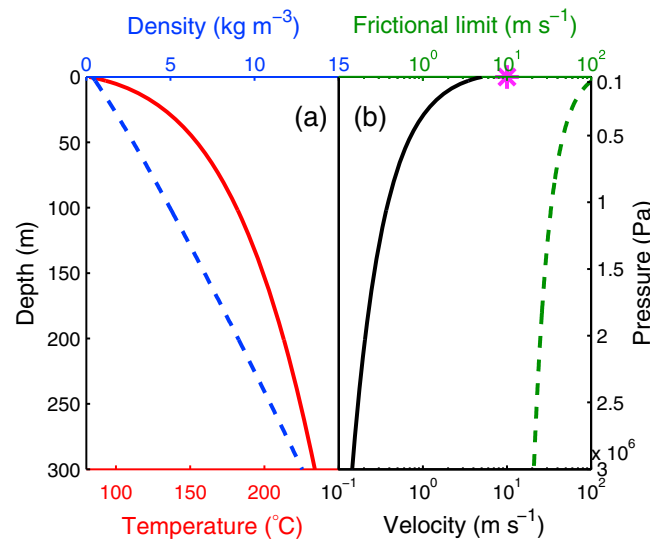


Figure 11. (a) Red curve and broken, blue lines show vertical profiles of boiling temperature and steam density, respectively, assuming hydrostatic pressure, $P = \rho_1 gz$, and $\rho_1 = 10^3 \text{ kg m}^{-3}$. (b) Black and broken, green curves are estimated velocity profiles by equations (19) and (20), respectively, using conditions shown in Figure 11a. Pink asterisk shows the order of magnitude of observed velocity. The colors of the curves correspond to their reference axes.

where D is the typical width of the conduit through which the steam flows, and f is a friction factor. Using the classic empirical turbulent model of Blasius, f is estimated by

$$f = 0.3164 Re^{-1/4}, \quad (21)$$

where Re is the Reynolds number [Turcotte and Schubert, 2002]. This model works well for smooth fractures [Button *et al.*, 1978]. Assuming $U_g \sim 10 \text{ m s}^{-1}$, $f \sim 0.03$. For rough fractures, f increases. We use $f = 0.07$, corresponding to roughness length scales 5% of the fracture width [Moody and Princeton, 1944]. Assuming that the dynamic pressure gradient balances the hydrostatic pressure gradient, $dP/dz \sim 10^4 \text{ Pa m}^{-1}$, and the width of the conduit $D \sim 20 \text{ mm}$, which is twice the vent width and is a maximum assumption, we obtain the velocity of frictional flow and denote it by the broken, green curve in Figure 11b.

The calculated velocity at the vent is one order of magnitude higher than the observed discharge velocity, despite the fact that D is twice the observed width at the vent, $D \sim 20 \text{ mm}$. We thus infer that frictional flow can regulate the ascent in the conduit and maintain the high pressure inside the conduit.

Choking at the vent has been suggested by Kieffer [1989] because of the slow sound velocity of the steam and liquid water mixture, and that hypothesis has been tested by a field experiment at Lone Star Geyser, Yellowstone National Park [Karlstrom *et al.*, 2013]. Karlstrom *et al.* [2013] compared the measured discharge velocity with the sound velocity estimated from possible liquid/steam fractions, assuming isentropic flow and taking into account the entrainment effect, and concluded that flow is likely choked at the vent. The temperature and pressure conditions estimated in El Cobreloa are similar to those in Lone Star Geyser. Thus, choking is another possible mechanism to regulate steam flow at the vent and maintain high pressure inside the conduit.

Because of the restricted discharge from the vent and heat supply from below, the pressure inside the conduit and reservoir may become superhydrostatic. Higher pressure may reduce the volumetric flux into the reservoir from below, prolonging the steam-dominated phase of the eruption.

In summary, permeability is estimated from the volume and duration of the steam-dominated eruption, source flux is estimated from the duration of minor eruptions, and the temperature of the surrounding aquifer is estimated from the time interval of minor eruptions. These estimates provide values that can be used in solving the conservation equations presented in section 5.3.

5.5. Numerical Simulations of Intermittent Eruptions

The evolution of an eruption is governed by the time integration of equations (1)–(15). Here we perform this integration using small modifications to the parameters estimated in the previous section, as summarized in Table 1. Figure 12 shows the evolution of conditions inside the reservoir during two boiling events. We adopt $T_r = T_b$ and $h_r = h_1$ as initial conditions, i.e., the water in the reservoir has just reached the boiling temperature.

Figure 12a shows that, in the reservoir, enthalpy per unit mass increases as heat is supplied from below. The temperature in the reservoir remains constant, however, because heat is used for vaporization (Figure 12b). As a result, the liquid fraction in the reservoir decreases (Figure 12c). Because the water in the reservoir is boiling, the source fluid is supplied as steam and q_1 is high, as shown by the green line in Figure 12d.

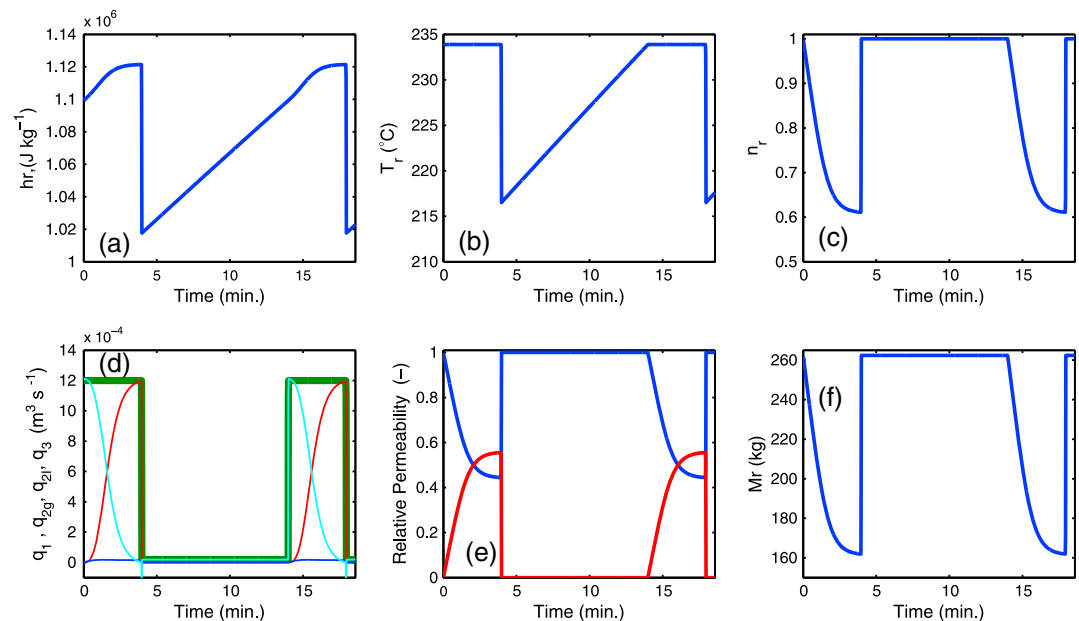


Figure 12. (a) Time evolution of enthalpy per unit mass in the reservoir. (b) Time evolution of temperature within the reservoir. (c) Time-dependent volumetric liquid saturation. (d) The volume fluxes q_1 (green), q_{2g} (red), q_{2l} (blue), and q_3 (light blue). (e) Relative permeabilities for liquid (blue) and gas (red) phases. (f) Time evolution of mass within the reservoir.

Accordingly, the volume flux to the surrounding aquifer is high, as shown by the light blue curve in Figure 12d.

The volume flux from the reservoir to the upper conduit increases with the steam fraction in the reservoir, as shown by the red and blue curves in Figure 12d. We attribute the minor eruptions to this flux of steam (Figure 8b). The volume flux of steam q_{2g} from the reservoir to the conduit is much larger than that of liquid phases, q_{2l} . This is because the viscosity of steam is lower than that of liquid phase by two orders of magnitude. The relative permeability, which also controls this flux, depends on the saturation in the reservoir, as shown in Figure 12e.

When the steam fraction in the reservoir increases, the flux from the reservoir to the upper conduit exceeds the flux from the source, $q_1 < q_2$. As a result, liquid water in the surrounding aquifer flows into the reservoir, as shown by the light blue curve in Figure 12d. Because the water flowing into the reservoir from the surrounding aquifer is colder than the reservoir, the reservoir is cooled to below the boiling temperature (Figure 8c, section 5.2, item 7). The mass in the reservoir increases, since the steam is replaced by liquid, as shown in Figure 12f. The lowest temperature in the reservoir is 217°C and is higher than the assumed aquifer temperature of 181°C. This is because not all of the reservoir water is replaced by the aquifer water, and our initial condition plots on the line for 217°C in Figure 10. The supply of source hot fluid heats the reservoir until it boils, as shown in Figures 12a, 12b, and 8a. During this stage, the source hot fluid is supplied in a liquid state so that the volume fluxes are low, as shown in Figure 12d.

The characteristics of steam flux shown by the red curve in Figure 12d are consistent with the observed characteristics of minor eruptions. The minor eruption is not the release of a single gas slug but the intermittent release of many bubbles over a 4 min period. Minor eruptions begin with small gas emissions, and the height of the splashes increases with time, before ending abruptly.

Figure 13 shows integrations with the same conditions as Figure 12 but over a greater number of eruptions. Minor eruptions occur regularly, as shown in Figures 13a–13c.

The cumulative steam flux increases with each minor eruption and would heat water in the conduit. We calculate the possible temperature rise in the conduit when 10% (blue) and 50% (green) of the heat in the steam slugs is added to the liquid in the conduit (Figure 13d), assuming that the conduit is initially filled with water at 87°C. Minor eruptions are expected to become more vigorous, as observed, because the conduit becomes progressively warmer.

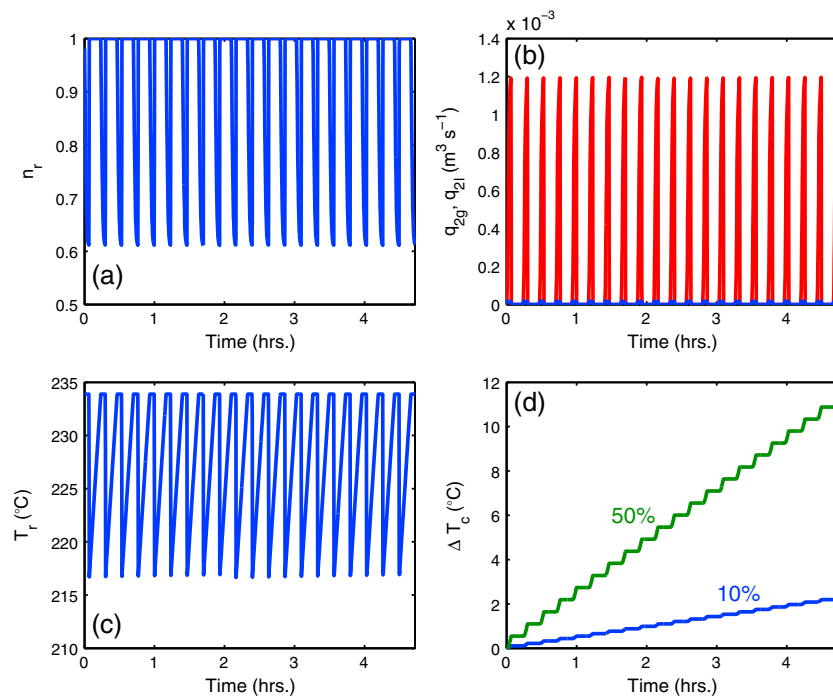


Figure 13. (a) Time-dependent volumetric liquid saturation in the reservoir. (b) The volume fluxes of steam (red curve) and liquid (blue curve) water flowing out from the reservoir to the upper conduit. (c) Time-dependent temperature in the reservoir. (d) Possible temperature rise in the conduit by the ascending steam slugs. We here assume 10% (blue curve) and 50% (green curve) of heat in the slug is used to heat water within the conduit.

After a sufficient number of minor eruptions, water in the upper parts of the conduit approaches the boiling temperature (section 5.2, item 8). At this point, the splashing of water during the next minor eruption can cause water in the conduit to boil owing to the pressure decrease (section 5.2, item 11). Unloading of deeper water in the conduit can cause the boiling surface to progressively move downward, an eruption mechanism proposed by *Bunsen* [1847] based on his measurements in Iceland. Boiling in the conduit ejects both steam and liquid water. The next minor eruption would deliver still more enthalpy to the conduit, and the observations shown in Figure 5 suggest that this influences the transition to a steam-dominated eruption.

Eventually, the conduit empties and the pressure inside the conduit is low, so that surrounding cold water flows into the conduit (Figure 8f, section 5.2, item 12). The height of the water column in the conduit may remain approximately constant between the major eruptions.

The evolution of the mass fraction of liquid water and steam during the eruption, and the temperatures between eruptions, are similar to those in the numerical simulations of *Ingebritsen and Rojstaczer* [1993, 1996] who solved the full partial differential equations for heat, mass, and momentum transport in porous media where the flow is governed by a two-phase Darcy model. The governing equations here are essentially the same, so even though we assume the geometry shown in Figure 8 and simplified the calculation, we should expect similar behavior.

5.6. Relation Between the Minor Eruption and Preplay Events at Other Geysers

The minor eruptions we observed at El Cobreloa bear some similarity to events termed “preplay” at geysers in Yellowstone National Park, in which puffs of steam and small volumes of liquid water are discharged from the vent [*Kieffer, 1989; Karlstrom et al., 2013*]. At El Cobreloa, the minor eruptions differ from these preplay events only in that they are periodic. However, at Yellowstone, deeper periodic processes recorded by tiltmeters that are interpreted as the motion of gas slugs (*J. Vandemeulebrouck et al., Eruptions at Lone Star Geyser, Yellowstone National Park, USA, Part 2: Geophysical constraints on subsurface dynamics, submitted to Journal of Geophysical Research, 2014*) may be analogous to the regular release of steam from our reservoir.

The thermal consequence of preplay events is to remove cold liquid water from the conduit and to deliver latent heat to the remaining water, raising conduit temperature. If the water in the shallow conduit reaches the boiling temperature, we expect vigorous eruptions. Boiling at the top of the water column removes mass, thus boiling underlying water [Bunsen, 1847]. This positive feedback may allow vigorous and sustained eruption. Removal of cold water at the top of the conduit by preplay can trigger major eruptions, and the timing of the minor and major eruptions at El Cobreloa appears to document this interaction. A major eruption will not result if the water in the conduit or surface pool never reaches the boiling temperature. Indeed, there are several geysers at El Tatio that display eruption styles that resemble only what we term minor eruptions: eruptions driven by steam released at depth.

6. Conclusion

Based on field measurements at the El Cobreloa geyser in the El Tatio geyser field, Chile, we identified two distinct eruption styles: less energetic minor eruptions and vigorous major eruptions. The latter begin with a liquid water-dominated eruption that transitions to a steam-dominated eruption. We developed a model for El Cobreloa taking into account insights and constraints from geothermal drilling. The upper and lower conduit of El Cobreloa is surrounded by cold and hot water, respectively, and a reservoir exists in the lower conduit at a depth of approximately 300 m. Magmatically heated fluid is supplied from below the reservoir and causes water in the reservoir to boil, creating minor eruptions. Minor eruptions deliver enthalpy to the upper conduit. When water in the upper conduit is hot enough, major eruptions can begin and are sustained.

Here we have used information from drilling and local geology to constrain the depths of the various reservoirs and water sources. However, the conceptual model and numerical results apply for systems with reservoirs at all depths, including the shallow depths inferred at some other geysers [e.g., Belousov *et al.*, 2013; Vandemeulebrouck *et al.*, 2013]. The key feature of the conceptual model and its formulation is the existence of a reservoir that begins to deliver water to conduit once sufficient steam accumulates.

The minor eruptions observed at El Cobreloa resemble preplay documented at other geysers. The most important role of preplay is removing cold water at the top of the conduit and heating the rest of the conduit, creating conditions that allow the major eruption to occur. Minor eruptions in El Cobreloa differ from preplay at other geysers by being periodic.

Acknowledgments

We thank the Geyser Team (in alphabetical order): Shaul Hurwitz, Eric King, Angello Negri, Pablo Ortega, Ameeta Patel, Maxwell Rudolph, and Chi-Yuen Wang. Some of the instruments were provided by Satoshi Ide, Jun Oikawa, and Atsushi Watanabe. We thank Steve Ingebritsen and an anonymous reviewer for their helpful and detailed review and comments. Financial support was provided by the KAKENHI24681035, NSF, and CONICYT. A.N. was sent to Chile by the OIYR Program.

References

- Belousov, A., M. Belousova, and A. Nechayev (2013), Video observations inside conduits of erupting geysers in Kamchatka, Russia, and their geological framework: Implications for the geyser mechanism, *Geology*, *41*, 387–390, doi:10.1130/G33366.1.
- Bryan, T. S. (2005), *Geysers: What They are and How They Work*, 69 pp., Mountain Press Publ. Company, Missoula, Mont.
- Bunsen, R. (1847), Physikalische Beobachtungen über die hauptsächlichsten Geysir Islands, *Annalen der Physik und Chemie*, *83*, 159–170.
- Button, B. L., A. F. Grogon, T. C. Chivers, and P. T. Manning (1978), Gas flow through cracks, *J. Fluids Eng.*, *100*, 453–458.
- Corey, A. T. (1957), Measurement of water and air permeability in unsaturated soil, *Proc. Soil Sci. Soc. Am.*, *21*, 7–10.
- Cortecci, G., T. Boschetti, M. Mussi, C. H. Lameli, C. Mucchino, and M. Barbieri (2005), New chemical and original isotopic data on waters from El Tatio geothermal field, northern Chile, *Geochem. J.*, *39*, 547–571.
- Cros, E., P. Roux, J. Vandemeulebrouck, and S. Kedar (2011), Locating hydrothermal acoustic sources at Old Faithful Geyser using Matched Field Processing, *Geophys. J. Int.*, *187*, 385–393.
- Cusicanqui, H., W. A. J. Mahon, and A. J. Ellis (1975), The geochemistry of the El Tatio Geothermal Field, Northern Chile, *Second United Nations Symposium on the Development and Utilization of Geothermal Resources*, pp. 703–711, San Francisco.
- Giggenbach, W. F. (1978), The isotopic composition of waters from the El Tatio geothermal field, Northern Chile, *Geochim. Cosmochim. Acta*, *42*, 979–988.
- Hayashi, M., et al. (2013), *Chronological Scientific Tables*, 984 pp., National Astronomical Observatory, Maruzen Co., Ltd., Japan.
- Healy, J., and M. P. Hochstein (1973), Horizontal flow in hydrothermal systems, *J. Hydrol.*, *12*, 71–82.
- Hurwitz, S., A. Kumar, R. Taylor, and H. Heasler (2008), Climate-induced variations of geyser periodicity in Yellowstone National Park, USA, *Geology*, *36*, 451–454.
- Hurwitz, S., R. A. Sohn, K. Luttrell, and M. Manga (2014), Triggering and modulation of geyser eruptions in Yellowstone National Park by earthquakes, Earth tides, and weather, *J. Geophys. Res. Solid Earth*, *119*, 1718–1737, doi:10.1002/2013JB010803.
- Husen, S., R. Taylor, R. B. Smith, and H. Heasler (2004), Changes in geyser eruption behavior and remotely triggered seismicity in Yellowstone National Park produced by the 2002 M 7.9 Denali fault earthquake, Alaska, *Geology*, *32*, 537–540.
- Hutchinson, R. A., J. A. Westphal, and S. W. Kieffer (1997), In situ observations of Old Faithful Geyser, *Geology*, *25*, 875–878.
- Ingebritsen, S. E., and S. A. Rojstaczer (1993), Controls on geyser periodicity, *Science*, *262*, 889–892.
- Ingebritsen, S. E., and S. A. Rojstaczer (1996), Geyser periodicity and the response of geysers to deformation, *J. Geophys. Res.*, *101*, 21,891–21,905.
- Ingebritsen, S. E., W. E. Sanford, and C. E. Neuzil (2006), *Groundwater in Geologic Processes*, 536 pp., Cambridge Univ. Press, Cambridge, U. K.

- Karlstrom, L., S. Hurwitz, R. Sohn, J. Vandemeulebrouck, F. Murphy, M. L. Rudolph, M. J. S. Johnston, M. Manga, and R. B. McCleskey (2013), Eruptions at Lone Star Geysers, Yellowstone National Park, USA: 1. Energetics and eruption dynamics, *J. Geophys. Res. Solid Earth*, *118*, 4048–4062, doi:10.1002/jgrb.50251.
- Kedar, S., B. Sturtevant, and H. Kanamori (1996), The origin of harmonic tremor at Old Faithful geyser, *Nature*, *379*, 708–711.
- Kedar, S., H. Kanamori, and B. Sturtevant (1998), Bubble collapse as the source of tremor at Old Faithful Geysers, *J. Geophys. Res.*, *103*, 24,283–24,299.
- Kieffer, S. W. (1984), Seismicity of Old Faithful geyser: An isolated source of geothermal noise and possible analogue of volcanic seismicity, *J. Volcanol. Geotherm. Res.*, *22*, 59–95.
- Kieffer, S. W. (1989), Geologic nozzles, *Rev. Geophys.*, *27*, 3–38.
- Lahsen, A. (1976), La actividad geotermal y sus relaciones con la tectonica y el volcanismo en el norte de Chile, *Actas, I Congreso Geologico Chileno*, *1*, B105–B127, Antofagasta.
- Lu, X., and S. W. Kieffer (2009), Thermodynamics and mass transport in multicomponent, multiphase H₂O systems of planetary interest, *Annu. Rev. Earth Planet. Sci.*, *37*, 449–77.
- Manga, M., and E. Brodsky (2006), Seismic triggering of eruptions in the far field: Volcanoes and geysers, *Annu. Rev. Earth Planet. Sci.*, *34*, 263–91.
- Manga, M., I. Beresnev, E. E. Brodsky, J. E. Elkhoury, D. Elsworth, S. E. Ingebritsen, D. C. Mays, and C.-Y. Wang (2012), Changes in permeability by transient stresses: Field observations, experiments and mechanisms, *Rev. Geophys.*, *50*, RG2004, doi:10.1029/2011RG000382.
- Moody, L. F., and N. J. Princeton (1944), Friction factors for pipe flow, *Trans. ASME*, *66*, 671–684.
- Munoz, M., and V. Hamza (1993), Heat flow and temperature gradients in Chile, in *Proceedings of International Meeting on Terrestrial Heat Flow the Lithosphere Structure, Bechyně Castle*, vol. 37, edited by V. Cermák, pp. 315–348, Special Issue Studia geoph. et geod., Prague, Czech Republic.
- Nishimura, T., M. Ichihara, and S. Ueki (2006), Investigation of the Onikobe geyser, NE Japan, by observing the ground tilt and flow parameters, *Earth Planets Space*, *58*, e21–e24.
- O'Hara, K. D., and E. K. Esawi (2013), Model for the eruption of the Old Faithful geyser, Yellowstone National Park, *Geol. Soc. Am.*, *23*, 4–9.
- Rojstaczer, S., D. L. Galloway, S. E. Ingebritsen, and D. M. Rubin (2003), Variability in geyser eruptive timing and its causes: Yellowstone National Park, *Geophys. Res. Lett.*, *30*, 1953, doi:10.1029/2003GL017853.
- Rudolph, M. L., M. Manga, S. Hurwitz, M. Johnston, L. Karlstrom, and C.-Y. Wang (2012), Mechanics of Old Faithful Geysers, California, *Geophys. Res. Lett.*, *39*, L24308, doi:10.1029/2012GL054012.
- Shteinberg, A., M. Manga, and E. Korolev (2013), Measuring pressure in the source region for geysers, Geyser Valley, Kamchatka, *J. Volcanol. Geotherm. Res.*, *264*, 12–16.
- Steinberg, G. S., A. G. Merzhanov, and A. S. Steinberg (1981), Geyser process: Its theory, modeling, and field experiment Part 1. Theory of the geyser process, *Mod. Geol.*, *8*, 67–70.
- Steinberg, G. S., A. G. Merzhanov, A. S. Steinberg, and A. A. Rasina (1982), Geyser process: Its theory, modeling, and field experiment Part 2. A laboratory model of a geyser, *Mod. Geol.*, *8*, 71–74.
- Tassi, F., C. Martinez, O. Vaselli, B. Capaccioni, and J. Viramonte (2005), Light hydrocarbons as redox and temperature indicators in the geothermal field of El Tatio (northern Chile), *Appl. Geochem.*, *20*, 2049–2062.
- Tassi, F., F. Aguilera, T. Darrah, O. Vaselli, B. Capaccioni, R. J. Poreda, and A. D. Huertas (2010), Fluid geochemistry of hydrothermal systems in the Arica-Parinacota, Tarapaca and Antofagasta regions (northern Chile), *J. Volcanol. Geotherm. Res.*, *192*, 1–15.
- Toramaru, A., and K. Maeda (2013), Mass and style of eruptions in experimental geysers, *J. Volcano. Geotherm. Res.*, *257*, 227–239.
- Turcotte, D., and G. Schubert (2002), *Geodynamics*, 456 pp., Cambridge Univ. Press, New York.
- Urzua, L., T. Powell, W. B. Cumming, and P. Dobson (2002), Apacheta, a new geothermal prospect in Northern Chile, *Trans. Geotherm. Resour. Council*, *26*, 65–69.
- Vandemeulebrouck, J., D. Stemmelen, T. Hurst, and J. Grangeon (2005), Analogue modeling of instabilities in crater lake hydrothermal systems, *J. Geophys. Res.*, *110*, B02212, doi:10.1029/2003JB002794.
- Vandemeulebrouck, J., P. Roux, P. Gouédard, A. Legaz, A. Revil, A. W. Hurst, A. Bolève, and A. Jardani (2010), Application of acoustic noise and self-potential localization techniques to a buried hydrothermal vent (Waimangu Old Geysers site, New Zealand), *Geophys. J. Int.*, *180*, 883–890.
- Vandemeulebrouck, J., P. Roux, and E. Cros (2013), The plumbing of Old Faithful Geysers revealed by hydrothermal tremor, *Geophys. Res. Lett.*, *40*, 1989–1993, doi:10.1002/grl.50422.